

Cluster Difference Imaging Photometric Survey. III. An Open Cluster With a 300 pc Halo

L. G. BOUMA,¹ J. L. CURTIS,^{2,3} J. D. HARTMAN,¹ J. N. WINN,¹ AND G. Á. BAKOS¹

¹Department of Astrophysical Sciences, Princeton University, 4 Ivy Lane, Princeton, NJ 08540, USA

²Department of Astronomy, Columbia University, 550 West 120th Street, New York, NY 10027, USA

³Department of Astrophysics, American Museum of Natural History, Central Park West, New York, NY 10024, USA

(Received —; Revised —; Accepted —)

Submitted to ApJL.

ABSTRACT

Recent analyses of the Gaia data have reported the existence of diffuse stellar populations surrounding nearby open clusters. The stars in these diffuse halos could be the tidal escapees of the cluster cores, or they could be remnants of an initially dispersed star formation complex. They could also be field stars—the false positives of overly aggressive clustering algorithms. In this study, we focus on a halo with a length of 300 pc reported around the ≈ 175 Myr open cluster NGC 2516. The classical tidal radius of the cluster is ≈ 10 pc. Combining photometry from Gaia, rotation periods from TESS, and lithium measurements from Gaia-ESO and GALAH, we find that the halo of NGC 2516 is real and coeval with the core. Two in three kinematically selected halo members 25–250 pc from the cluster center show rotation periods consistent with a gyrochronological age of 120 Myr. A comparison sample of field stars shows no such trend. The rotation period and lithium abundances of the cluster stars are also anti-correlated at fixed stellar mass, as has been observed in similar stellar populations. This work expands the set of confirmed NGC 2516 members by a factor of ≈ 2 , and quantifies the degree to which Gaia-based analyses can identify dispersed stellar populations against a background of field star contaminants. We highlight the implications for spectroscopic survey targeting, open cluster dispersal, and planet searches around young stars.

Keywords: stellar ages (1581), stellar associations (1582), open clusters (1160), stellar rotation (1629)

1. INTRODUCTION

Star clusters form in hierarchically structured molecular clouds (Shu et al. 1987). Over the first 10 Myr, “feedback” effects including protostellar outflows, photoionization, radiation pressure, and supernova shocks disperse the gas out of the cloud (Krumholz et al. 2019). Since only a small fraction of the cloud mass is converted into stars ($\sim 1\%$), gas dispersal enables the majority ($\sim 90\%$) of stars in the cluster to escape the cluster’s gravitational well (Lada & Lada 2003).

From 10 to 1000 Myr, the cluster remnants that survive gas dispersal suffer an onslaught that almost always leads to dissolution. Within the cluster supernovae, AGB winds, and close stellar encounters lead to additional mass loss (Lamers et al. 2010). Extrinsic to the cluster, collisions with giant molecular clouds (Spitzer 1958), and perturbations from the galactic tide in both the radial and vertical dimensions further promote stellar escape (e.g., Fukushige & Heggie 2000; Bergond et al. 2001).

Finding the stars that have dispersed from their natal clusters into the galactic field is of interest for a few reasons. One is to understand the predominant conditions under which stars and star clusters form (e.g., Wright & Mamajek 2018). Another is to understand the Sun’s birth environment (Adams 2010). Did the Sun form in an open cluster, and if so, what type? Is there any hope at identifying the stars that formed near the Sun? Open clusters and their dispersed remnants also provide a test case for “chemical tagging” (Freeman & Bland-Hawthorn 2002; Hogg et al. 2016; Ness et al. 2018, e.g.). The converse holds too: one could use chemical tagging to test the viability of kinematic clustering methods.

A separate project that benefits from the new discoveries of dispersed stellar populations is that of finding young transiting exoplanets. Young transiting planets are hard to find because young stars are rare, and mostly reside in crowded galactic plane (see e.g., Kharchenko et al. 2013; Piskunov et al. 2018). If the dispersed halos of nearby star clusters could be reliably identified, this could expand the census of nearby young stars by up to a factor of 10, based on the expected fraction of stars thought to be lost during gas dispersal.

The detection of dispersed stellar associations, although possible before Gaia, has now reached a breakthrough pace (e.g., Bergond et al. 2001; Zuckerman & Song 2004; Oh et al. 2017; Cantat-Gaudin et al. 2018; Gagné et al. 2018; Gagné & Faherty 2018; Kounkel et al. 2018; Zari et al. 2018; Kounkel & Covey 2019; Fürnkranz et al. 2019). The results can be summarized as follows. On one end are coeval populations with no discernable cores (e.g., Psc Eri and μ Tau, Meingast et al. 2019; Curtis et al. 2019; Gagné et al. 2020). On the other are hierarchically structured populations with many over and under-densities (e.g. the Sco-Cen and Vela OB2 associations Pecaut & Mamajek 2016; Cantat-Gaudin et al. 2019). Here, we focus on the middle: low-density halos associated with a single overdensity, typically an open cluster that was known before Gaia (see Kounkel & Covey 2019; Kounkel et al. 2020; Meingast et al. 2021). In some cases, these halos could correspond to tidal tails, as have been reported in the Hyades (Meingast & Alves 2019; Röser et al. 2019), the Ursa Major moving group (Gagné et al. 2020), and in Coma Berenices (Tang et al. 2019).

One point of difficulty however is that different clustering methods yield differing levels of both sensitivity and precision (Hunt & Reffert 2020). Using say a Gaussian Mixture Model tautologically yields open clusters that are elliptical (e.g., Wallace 2018). Some unsupervised methods yield dispersed and asymmetric structures with number densities down to 100 times less than the field around the same regions (see e.g. Kounkel & Covey 2019, hereafter KC19], and Meingast et al. 2021, hereafter M21). Discrepancies between different clustering methods leads to the question of how contaminated the resulting samples are, and in some cases whether the reported structures are truly coeval stellar populations.

We have recently been making TESS light curves of stars reported to be members of such populations (CDIPS, Bouma et al. 2019a). Our analysis of TESS Cycle 1 (Sectors 1-13) yielded light curves of 483,407 candidate cluster members in the Southern Ecliptic hemisphere, available on MAST¹.

As part of this broader project, we focus here on a modest question: in just a single rich southern open cluster, is the cluster halo truly coeval with the core? We chose NGC 2516 for this analysis since it is young (≈ 120 Myr) and sufficiently nearby ($d \approx 400$ pc) to facilitate photometric rotation measurements using TESS, and some degree of spectroscopic analysis. Its halo is decidedly non-spherical: KC19 reported its dimensions as $\approx 20 \times 10 \times 350$ pc. We want to know: is the halo real? To what extent can we use Gaia alone to reliably identify age-dated needles in the haystack of field stars? What are the implications, observationally and theoretically, if we can identify the dispersed halos of open clusters?

A brief note on terminology. Low-density stellar associations connected to a dense population (the “core”) have been described as being in “halos”, “strings”, “coronae”, “snakes”, “the outskirts”, and “tidal tails” (e.g., Davenport & Sandquist

2010; Kounkel & Covey 2019; Röser et al. 2019; Tian 2020; Meingast et al. 2021). The latter term implies a particular model for the formation of the association. We opt to use “halo” because it is concise and model agnostic. It suffers however from the suggestion of spherical symmetry. The halo of NGC 2516 is anything but.

Section 2 summarizes the astrometric analyses of the Gaia data that led to our interest in NGC 2516. Section 3 age-dates the cluster’s halo and core using Gaia photometry (Section 3.1), TESS gyrochronology (Section 3.2), and lithium depletion (Section 3.3). In Section 4 we discuss the implications of our analysis for NGC 2516 specifically and stellar spin-down and open cluster evolution generally. Section 5 gives our conclusions.

2. A 300 PC HALO AROUND A CORE?

2.1. Gaia Astrometry

We selected candidate NGC 2516 members based on those available in the literature. While a number of pre-Gaia catalogs were available, the purity and accuracy of the Gaia-derived results are the current state of the art. We therefore adopted what we viewed as the most interesting clustering samples to compare: those of Cantat-Gaudin et al. (2018) (CG18), Kounkel & Covey (2019) (KC19), and Meingast et al. (2021) (M21). A useful visualization of these samples is available online². While we could have performed our own clustering analysis based on the Gaia data, such an effort would be only replicating the work of these investigators. We opt to instead use their studies as starting points.

CG18 reported 1106 candidate members of NGC 2516, brighter than $G = 18$ mag. Kounkel & Covey (2019) reported 3003 candidate members, and included stars up to ≈ 1 mag fainter. Finally, 1577 of the 1860 Meingast et al. (2021) sources (85%) were included in the Kounkel & Covey (2019) sample. Each study applied unsupervised clustering techniques to the second Gaia Data Release, as detailed in Appendix A.

CG18 considered a cone of radius **XX DEGREES** centered on the cluster’s position. Given the classically reported tidal radius of e.g., 9 pc, CITE Piskunov+2008, which is 8° at the cluster distance of ≈ 400 pc, perhaps they should have considered stars further out.

Figure 1 shows the cluster members reported by each study. The CG18 members are all within a few degrees of the cluster center, while the KC19 members span tens of degrees. In physical units, this corresponds to a size difference of XX pc versus YY pc. This difference is somewhat tautological, because CG18 did not extend their search for members out to tens of degrees from the cluster center, since their clustering algorithm relied on the contrast between cluster and field stars in the astrometric space of $(\mu_{\alpha'}, \mu_{\delta}, \pi)$. Nonetheless, the membership catalog of CG18 echoes that of many previous investigators (CITE, CITE, CITE), and is con-

¹ <https://archive.stsci.edu/hlsp/cdips>

² <https://homepage.univie.ac.at/stefan.meingast/coronae.html>, made by Meingast et al. (2021).

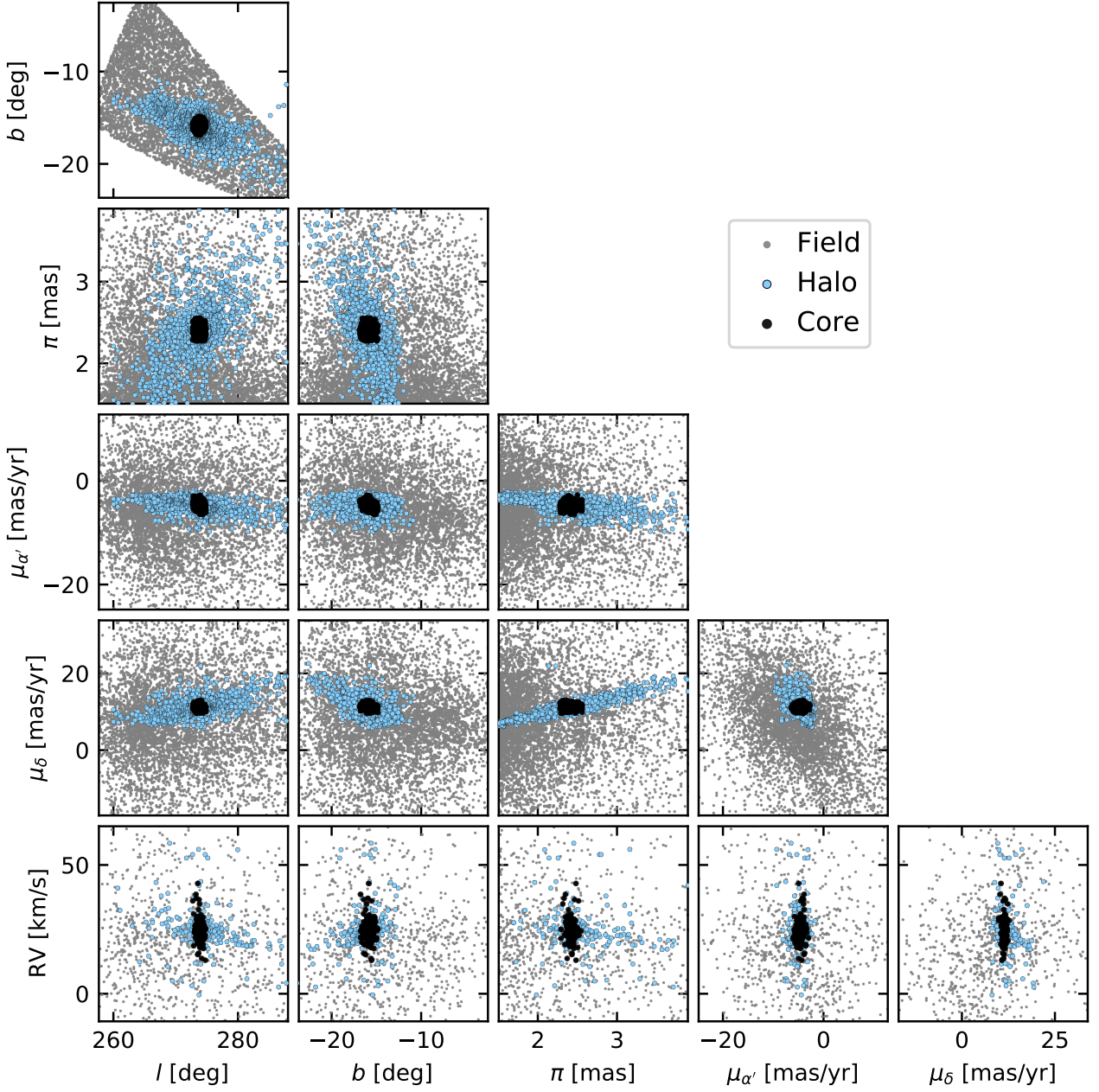


Figure 1. The dense and diffuse components of NGC 2516 across position and velocity space. The core (black) was identified by [Cantat-Gaudin et al. \(2018\)](#) using Gaia DR2, and is coincident with the visual overdensity of stars canonically accepted as “the cluster”. The halo (blue) was identified by [Kounkel & Covey \(2019\)](#) and [Meingast et al. \(2021\)](#) using less restrictive membership assignment algorithms described in Appendix A. The field sample is randomly drawn from a (α, δ, π) cube centered on the cluster. The low volume density of the halo stars makes it difficult to visually distinguish the field and halo samples.

sistent with the general *visual* impression that one has when looking at NGC 2516 visually: it seems to be at most X° , and not a big stream. This discrepancy begs the question. What is the true structure of NGC 2516? Are the core and halo truly coeval?

To answer these questions, we adopt the [CG18](#) stars as candidate “core” members and the [KC19](#) stars as candidate “halo” members. If a star is in both lists, it is a “core” member. 1091 of the 1106 core members are in both lists. This

leaves 1912 candidate members in the halo. Concatenating the two lists yields 3,018 candidate members.

In this work, we also define a set of nearby field stars in the “neighborhood” of NGC 2516. Based on the observed distribution of halo members, we draw these stars randomly from the following “cube” in right ascension, declination, and par-

allax:

$$\alpha [\text{deg}] \in [108, 132], \quad (1)$$

$$\delta [\text{deg}] \in [-76, -45], \quad (2)$$

$$\pi [\text{mas}] \in [1.5, 4.0]. \quad (3)$$

We imposed a magnitude limit of $G = 19$ mag, and ran the queries using the `astroquery.gaia` module (CITE). We allowed the number of stars in the comparison sample to exceed that in the cluster sample by a factor of ≈ 5 , to ensure broad sampling of stellar masses and evolutionary states. We also required the comparison sample to not overlap with the cluster sample, which led to the omission of 1.1% of the stars drawn over the volume noted above.

3. AGE-DATING THE HALO OF NGC 2516

3.1. HR Diagram from Gaia

The first check on the plausibility of the candidate cluster members being coeval was already performed by CG18, KC19, and M21. That check is to see whether the HR diagrams of the cluster members support the claim that they are coeval.

Figure 2 presents similar results to what these investigators have already found. The core members of the cluster show a clean sequence consistent with stars with a fixed age and metallicity, and varying mass. The halo members show a roughly consistent main-sequence, with somewhat greater scatter. One possible explanation for the additional scatter could be that the halo is more contaminated by field stars. For instance, ≈ 5 evolved halo stars are visible in the field-star portion of the red giant branch (RGB). Given the age of the system, these stars must be field interlopers.

A separate possible explanation for scatter in the halo's HR diagram could be differential reddening across different sightlines. The halo is reported to span 20° on-sky, and varies in position from about $b = -12^\circ$ to $b = -20^\circ$, with the stars closest to the galactic plane also being further from the Sun by up to 200 pc (Figure 1). Some empirical evidence for differential reddening is discussed further in Appendix D. Based on the available evidence, we expect that both field star contamination and differential reddening could play a role in the larger scatter of the halo relative to the core. A third possibility that we have not explored is whether the binary fraction could also differ between the different regions of the cluster.

In the right panel of Figure 2, we compare the observed photometry with PARSEC isochrones (Bressan et al. 2012; Chen et al. 2014, 2015; Marigo et al. 2017). We used the web interface³ to interpolate these isochrones at $\log_{10}(t/\text{yr}) = \{8, 8.25, 8.5\}$, and applied the reddening correction described in Section 3.2. We assumed a reddening of $E(B-V) = 0.102 \pm 0.019$, $R_V = 3.1$, and applyied the O'Donnell (1994) SED-dependent extinction law star-by-star

through the PARSEC interface. For the metallicity, we considered a range of super and sub-solar metallicities to fit as much of the locus from $0.5 < B_p - R_p < 1.5$ as possible, and settled on the slightly super-solar $[M/H] = 0.06$. Sub-solar metallicities led to model predictions too blue along the main sequence by ≈ 0.1 mag. Our adopted metallicity agrees with that found by Cummings (2011, Sec 4.4.4), and with the iron abundance recently determined by the Gaia-ESO team (Baratella et al. 2020), which represented an up-revision from an earlier sub-solar metallicity (Randich et al. 2018). While Bailey et al. (2018) report a slightly sub-solar metallicity for the cluster, we prefer super-solar based on the goodness of fit from the photometry.

Overall, the data and models agree for masses above approximately $0.45 M_\odot$. However below this mass, the data and models diverge at colors redder than $B_p - R_p \approx 2.2$. The MIST isochrones showed a comparable disagreement (Choi et al. 2016). Explanations invoking both starspots and incomplete molecular line lists have been proposed (e.g., Stauffer et al. 2003; Feiden & Chaboyer 2013; Rajpurohit et al. 2013; Mann et al. 2013; Choi et al. 2016). We adopt the PARSEC isochrones since they diverge at slightly lower mass than the MIST models, due to the temperature-opacity calibration implemented by Chen et al. (2014). For purposes of age-dating the cluster, we prefer to simply focus on the main-sequence turn-off (MSTO), since it is where the models have maximal predictive power.

Cummings & Kalirai (2018) presented techniques for mitigating some of the complexities of MSTO age-dating (e.g., sparse turnoffs, stellar rotation, high binarity fractions, and the presence of blue stragglers). Combining a *UBV* color-color analysis with Gaia DR2 cluster memberships, they found MSTO ages for NGC 2516 ranging from 165 to 195 Myr, depending on the choice of model isochrone (Y², PARSEC, MIST, or SYCLIST). The statistical uncertainties (≈ 25 Myr) were comparable to the systematic uncertainties.

Our primary goal is to determine whether the ages of the core and halo are consistent. The left panel of Figure 2 shows empirically that they are: stars past the turnoff in both the halo and core are on a consistent locus. The right panel of Figure 2 demonstrates the precision with which the claim can be made. The MSTO stars are consistent with the 178 and 316 Myr models, but are bluer than the 100 Myr model. The RGB stars are consistent only with the 178 Myr ($\log_{10} t/\text{yr} = 8.25$) model. Based on the assumption that the width of the MSTO can be attributed to binary stars, we are most interested in the blue edge. This appears most compatible with the 178 Myr model. These results are consistent with the MSTO age range of 165 to 195 Myr found by Cummings & Kalirai (2018), and we refer to their work for a more precise model-dependent comparison.

3.2. Rotation from TESS

3.2.1. Cluster Star Sample

First, we collected the 3,018 Gaia DR2 source_ids corresponding to the kinematically-identified core and halo mem-

³ <http://stev.oapd.inaf.it/cgi-bin/cmd>, 2021-02-26, CMD3.4, YBC bolometric corrections as in Chen et al. (2019).

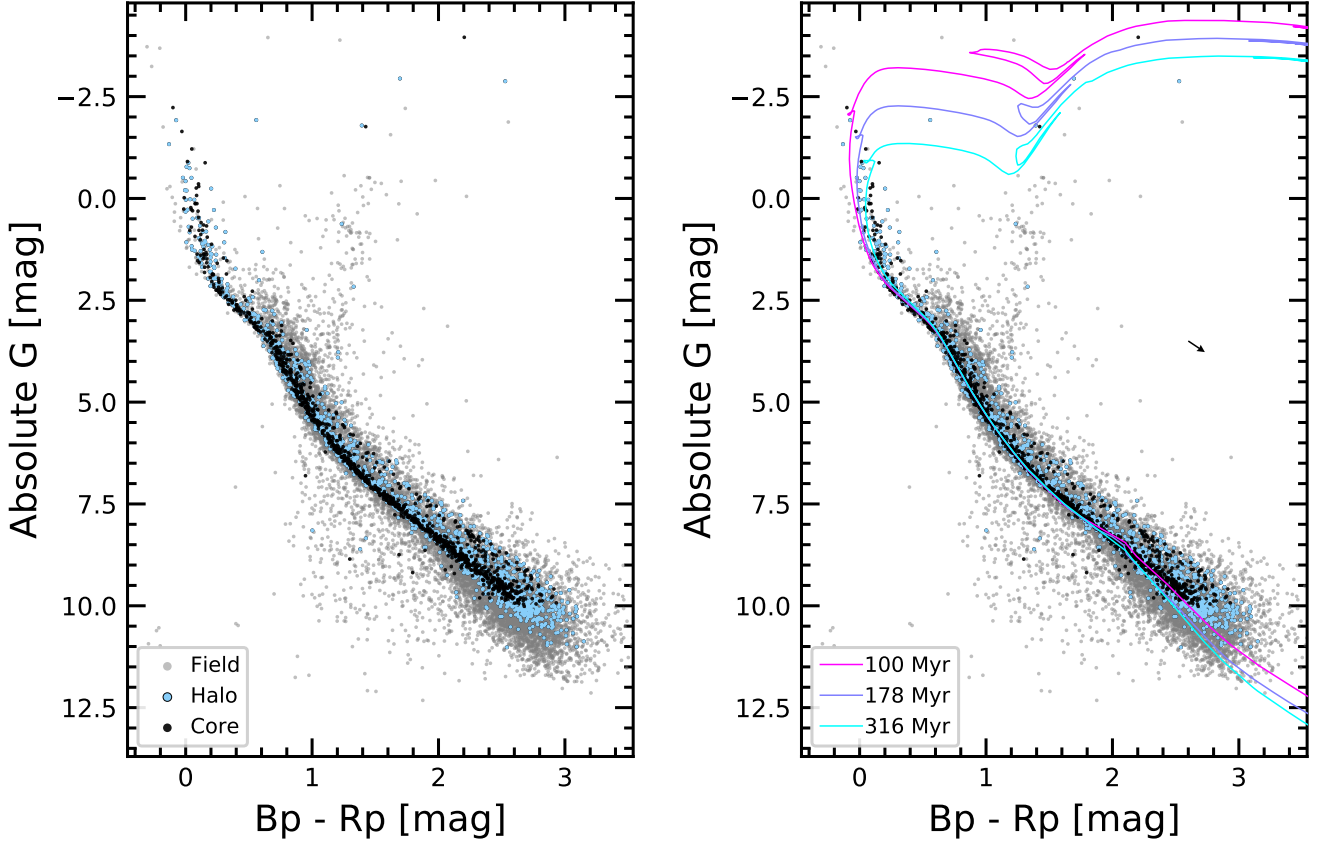


Figure 2. HR diagrams of NGC 2516. *Left:* Photometric data from Gaia EDR3; no reddening correction has been applied. The core (black) shows a main-sequence and turnoff consistent with stars of a fixed age and metallicity. The halo (blue) is similar, though the binary sequence is less defined. At fixed color, the faintest M dwarfs in the core and halo are brighter than in the field star comparison sample (gray), consistent with these stars not having yet reached the main-sequence. *Right:* PARSEC isochrones ($[Fe/H]=+0.06$) are overplotted at intervals of $\log_{10}(t/\text{yr}) = \{8, 8.25, 8.5\}$. The arrow represents the average reddening correction applied to the models. The main-sequence turn-off location and evolved stars suggests a cluster age slightly older than the Pleiades (dark blue line). The models diverge from the data for $M_* \lesssim 0.45M_\odot$ ($\approx M2V$; $Bp - Rp \approx 2.2$).

bers. For each source, we first retrieved all available CDIPS light curves, on a per-sector basis. This yielded 2,238 light curves, all brighter than $Rp = 16$ mag. The $Rp = 16$ mag cutoff imposed during the CDIPS processing corresponds roughly to $(Bp - Rp)_0$ of 2.2, or a spectral type of $\approx M2V$, at the distance of NGC 2516.

We cleaned and stitched the light curves as follows. First, we detrended the systematics in each sector individually, and stitched together the resulting light curves before searching for the periodicity. Some details regarding our detrending approach are discussed in Appendix B. After applying a detrending step aimed at removing systematic trends, we proceeded with a few small cleaning steps aimed at improving the purity of the rotation period measurements: we masked 0.7 days at the beginning and end of each spacecraft orbit, and ran a sliding standard-deviation rejection window over the light curve, which removed any outlying points within $\pm 3 \times \text{MAD}$ of the median in each window.

We then measured the rotation period of the resulting light curve. We used the the aperture radius that, based on theoret-

ical expectations, was expected to give the optimal balance between light from the target and background-light (CITE Sullivan15). This typically resulted in an aperture radius of either 1 or 1.5 pixels. To measure the periods, we used the periodogram implementations in astrobase, in particular the Stellingwerf PDM periodogram (CITE), along with the more traditional Lomb-Scargle (CITE). We recorded the top five periodogram peaks from each method, and their corresponding powers. Finally, as a check on crowding, we also recorded the number of stars within the aperture of equal brightness to the target stars, and of brightness with 1.25 and 2.5 TESS magnitudes of the target star.

Figure 3 shows the resulting rotation periods. The points on this plot are the 987 light curves for which the peak Lomb Scargle periodogram period was below 15 days, the LS power exceeded 0.08, and for which no equal-brightness or greater companions were within the aperture. We also required that at most one companion with brightness exceeding one tenth of the target star could reside in the aperture. These selection criteria are entirely heuristic, and yielded

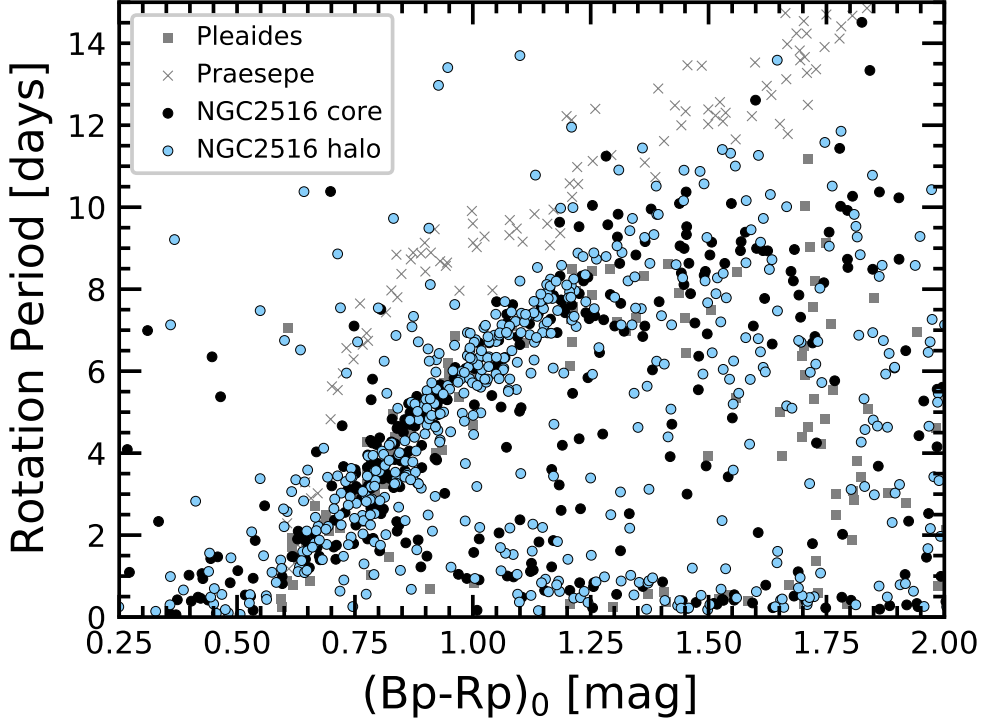


Figure 3. The core and halo of NGC 2516 in the space of rotation period and dereddened Gaia color. The Pleiades (125 Myr [Rebull et al. 2016](#)) and Praesepe (650 Myr [Douglas et al. 2017](#)) are shown for reference. Stars in the core and the halo of NGC 2516 appear gyrochronologically coeval with the Pleiades at $(Bp-Rp)_0 < 1.25$. There is a narrow range of color, from $1.25 < (Bp-Rp)_0 < 1.75$, in which some NGC 2516 members appear elevated with respect to the Pleiades, suggesting a slightly older age.

1,641 stars for which rotation periods might have been detected. By exploring the different possible selection criteria, we found that the ones we adopted provided a reasonable balance between excluding stars on the slow sequence, *vs.* reporting spurious rotation periods in the “void” below the slow sequence, where the dominant signal was in fact from a neighboring star. Splitting the resulting sample into the “core” and the “halo”, they suggest that the halo is real.

To put the clusters on the same color scale, we needed to adopt reddening corrections. We assumed X for the Pleiades, and Y for Praesepe. For NGC 2516, we queried the 2MASS DUST service to find the extinction parameters for the positions of each NGC 2516 member ([CITE: astrobase.services.dust; 2MASS DUST](#)). The mean and standard deviation of the $E(B-V)$ values for the Schlegel+98 and SF11 maps were consistent, so we considered those of Schlegel+1998: $E(B-V) = 0.206 \pm 0.039$. Bonifacio+2000 noted though that Schlegel+98 overestimate the reddening values when the color excess exceeds about 0.10 mag. We applied their correction (Eq 1 from Bonifacio+2000), which led to an adopted $E(B-V) = 0.102 \pm 0.019$. Finally, to convert to Gaia colors we adopted the calibration of Stassun et al 2019, and assumed $E(Bp-Rp) = 1.31E(B-V)$ and $A_G = 2.72E(B-V)$. This yielded $E(Bp-Rp) = 0.134 \pm 0.025$, which is used in the plots.

The resulting gyrochronology age we find for the core is XXX. For the halo, the claimed age from gyrochronology is

YYY. Applying the same procedure to the field star comparison sample (see Appendix C), we get an age of ZZZ+/-AAA.

3.2.2. Kinematics \otimes Rotation

How far away from the core, in position and velocity space, does the halo actually extend? We can explore this by cross-matching the rotator sample against 3,018 Gaia DR2 kinematic candidate members.

Figure 4 shows the result. An important nuance in interpreting this plot is that we show only stars with $0.5 < (Bp-Rp)_0 < 1.2$ for which our TESS pipeline successfully made detrended light curves. In other words—the base sample is the stars for which we could have plausibly detected a rotation period. Faint stars with $Rp > 16$ were beyond our light curve selection limit, and crowded stars (*e.g.*, near saturated stars in the cluster center) do not appear. We selected the color limit above based on Figure 3, since the density of period detections seems to decrease once $(Bp-Rp)_0 \gtrsim 1.25$, *i.e.*, for spectral types later than \approx K4V. Our expectation is that completion effects become important for fainter stars. At the distance of NGC 2516, a K4V star has $T \approx 14.5$, for which our reductions of the TESS images yield a precision of ≈ 7 mmag per half-hour exposure ([Bouma et al. 2019b](#)). **The AMPLITUDES of the rotation signals are like 10-100 mmag (CITE REBULL 2020, FIGURE 10).**

Qualitatively, the fraction of kinematic members with TESS-detected rotation periods seems like it may increase

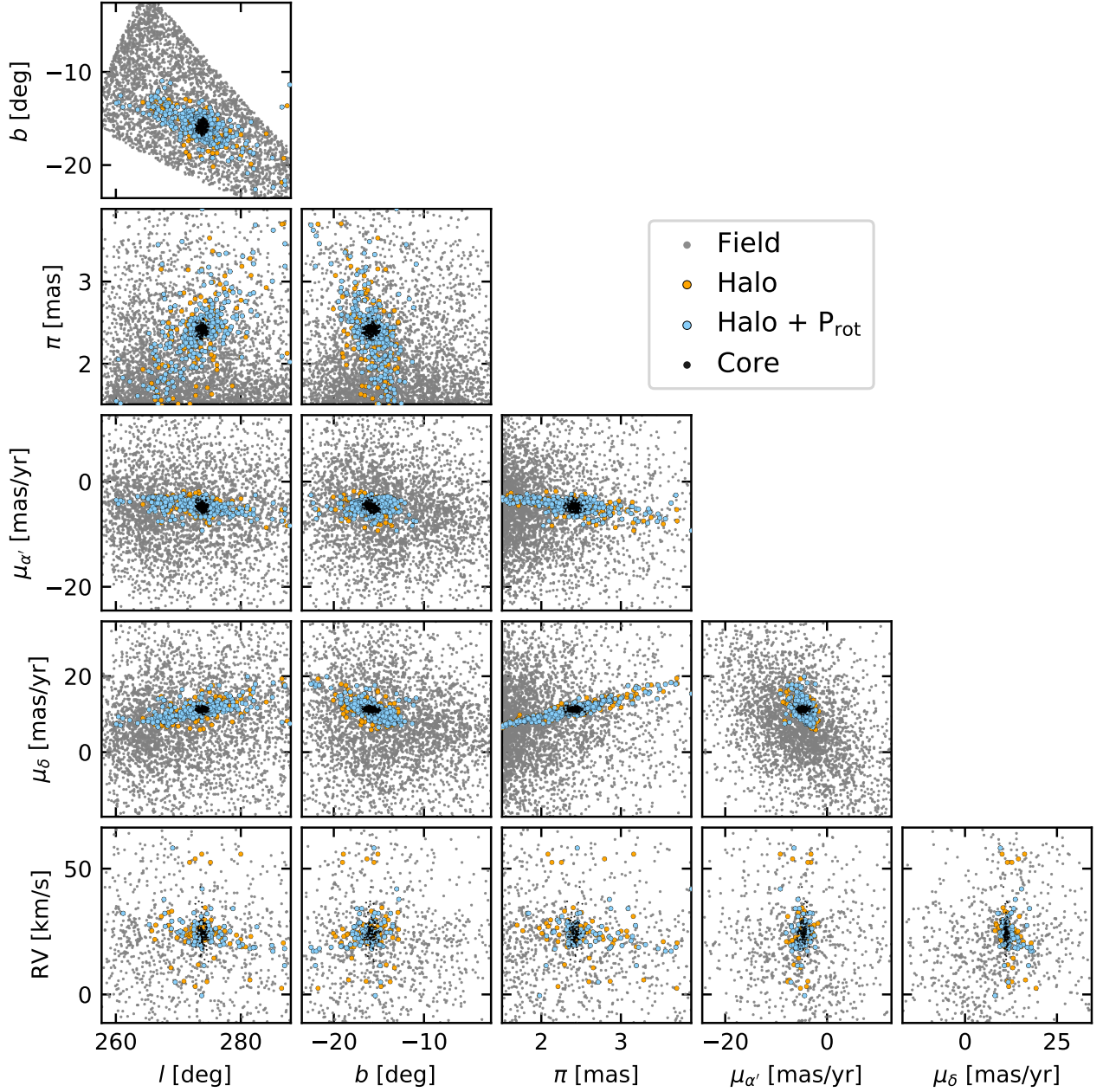


Figure 4. Gaia-based components of NGC 2516 in position and velocity space, cross-matched against the rotators. The plotted stars are those with $0.5 < (Bp - Rp)_0 < 1.2$ that meet the crowding restrictions described in Section 3.2: they should have been sufficiently bright and non-crowded to enable rotation period detection.

with increasing distance from the halo core—both in position and in velocity space. To quantify this, we computed the relevant distances in physical coordinates. This entailed first transforming from (α, δ, π) to galactocentric (X, Y, Z) which we did assuming the AstroPy v4.0 coordinate standard (CITE). We then converted the on-sky proper motions to physical units by dividing by the distance of each star. We then computed the SEPARATIONS of all of these positions and 2d-velocities from the “median core member”, which was selected by taking CG18 members with membership probability exceeding 70%. Again, we only considered

stars for which we could have plausibly detected a rotation period — the same color and observability limits discussed above were also applied.

The results are shown in Figure 5. The halo extends to separations of about 200 pc in physical space from the cluster core. This corresponds to a length of $\approx 300\text{-}350$ pc, depending on which members of the halo are chosen as the “tips” on either end.

In tangential velocity space, the fraction of stars with rotation period detections remains high out to roughly 10 km/s. Meingast et al. (2021) by comparison required a physically

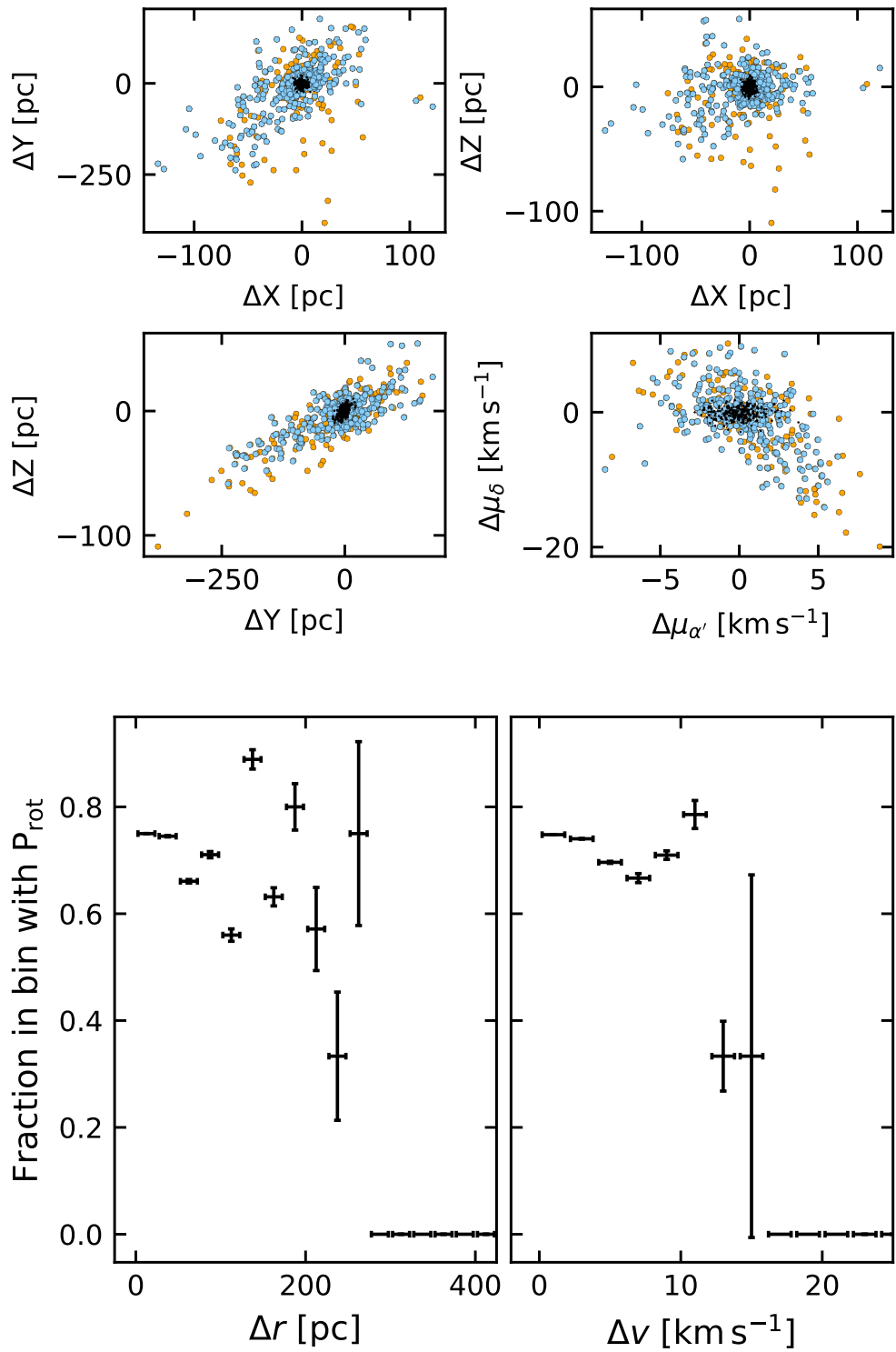


Figure 5. Gaia-based components of NGC 2516 in position and velocity space, cross-matched against the rotators, in physical units.
Top: projections in position and 2d-tangential velocity space. *Bottom:* radially binned versus 3d position and 2d velocity difference. Bins have width 25 pc in position, and 2.0 km s^{-1} in velocity.

motivated cut in tangential velocity space of 1.5 km per sec. This probably improves purity, but clearly doesn't get everything for completeness.

3.3. Lithium from Gaia-ESO and GALAH

The third and final approach we took for age-dating the stellar population was using the lithium depletion technique (CITE, CITE, CITE).

Reviewing the literature, two spectroscopic datasets for NGC 2516 seemed particularly important: Gaia-ESO (Randich et al. 2018) and GALAH DR3 (Buder et al. 2020). The target selection and results from each survey were as follows.

Gaia-ESO selected *cluster candidates* to be observed with the GIRAFFE and UVES spectrographs based on previously reported literature members and publicly available optical and NIR photometry. This target selection approach included many stars in the spatial proximity of previously known members. Since the possible existence of the NGC 2516 halo was not known at the time of targetting, very few “halo” stars are in their ultimate sample. For NGC 2516, Randich et al. (2018) ultimately reported stellar parameters (including lithium equivalent widths and metallicities) for 796 candidate members. Cross-matching against our kinematic list of 3,018 candidate members by position and imposing a 0.5'' maximum separation limit yields 492 kinematic members for which a Gaia-ESO spectrum was acquired and stellar parameters were reported. 15 of these (all with $(Bp - Rp)_0 > 2.0$) are spurious matches based on the Gaia color and GES effective temperature, and we remove them. This yields 477 stars, of which 436 are in the core, and 41 are in the halo. This ratio is primarily caused by the Gaia-ESO targetting selection function.

The GALAH DR3 target selection process is discussed in detail by Buder et al. (2020). The most relevant aspects for our project are that the “main” survey targeted $12.0 < V < 14.0$ stars at $\delta < +10^\circ$, provided the stars were at least ten degrees from the galactic plane. The survey is spatially inhomogeneous⁴. Special targeting for stars in the TESS southern continuous viewing zone, and for known open cluster members was also performed. We identified the candidate NGC 2516 members for which spectra had been obtained by searching the GALAH_DR3_main_allstar_v1 catalog, after excluding stars with the stellar parameter bit flags 1, 2, 3. This excludes spectra with unreliable broadening, low S/N, and unreliable wavelength solutions (see Table 6 of Buder et al. 2020). Since our main focus is measuring equivalent widths for the Li 6708 Å line, these were the most relevant bit flags for our purpose. Of our 3,018 candidate NGC 2516 members, 106 had spectra in GALAH DR3. 51 were in the “core”; 55 were in the “halo”. 77 had “finite” lithium, i.e., no lithium flag set.

We downloaded⁵ the GALAH DR3 spectra for all 106 entries. We then measured the lithium equivalent widths using PROCESS Y. We then concatenated the GALAH DR3 and Gaia-ESO results together.

Figure 6 shows the results. At fixed stellar mass (and age), the rapid rotators tend to show elevated lithium equivalent widths. This effect is mostly apparent in the K dwarfs. Similar trends in the Pleiades were noted nearly three decades ago by Soderblom et al. (1993). More recent studies have found comparable results in the Pleiades, the Psc-Eri stream, and M 35 (Bouvier et al. 2018; Arancibia et al. 2020; Jeffries et al. 2020). The fact that we see the same trend across the core and halo of NGC 2516 *a*) supports the conclusion that the halo is coeval with the core, and *b*) suggests that the lithium-rotation correlation is not explained by environmental effects such as the density of the cluster during its embedded phase, but is instead tied to physical processes acting on all low-mass pre-main-sequence stars.

Processes both internal and external to the star have been suggested to explain the lithium-rotation trend (CITE see the recent review by Bouvier+20). One explanation based in the stellar interior could be that the convective mixing efficiency is anticorrelated with the surface rotation (e.g., CITE Siess + Livio 1997, Baraffe+2017). Another possibility could be that stronger magnetic fields in the star’s interior inhibit convection (READ e.g., Ventura+98, Chabrier+07, Somers + Pinsonneault 2014). An external process that might also be important is the effect of star-disk magnetic locking during the PMS phase (CITE: magnetic braking). Longer disk lifetimes would lead to the star’s outer convective zone being locked for longer while the radiative core contracts. The resulting differential rotation and rotational mixing could drive the lithium depletion (CITE: Bouvier 08, Eggenberger+12). We have no preference between these possibilities—we simply note that the NGC 2516 sample could be another helpful data point in distinguishing them.

4. DISCUSSION

4.1. How did the halo form?

Another way to frame this question: should we call these stars a tidal tail? The classical explanation of such a structure (e.g., Krumholz+19) is that stars escape out of L1 and L2, and then form leading and lagging arms due to differential rotation in the galaxy. The leading and lagging arms of NGC 2516’s halo qualitatively match this picture, in that they are oriented roughly toward and away the direction of galactic rotation (CITE, Meingast21, link to their website).

A second explanation though invokes the idea that the cluster formed in a larger and lower-density star formation complex, and the stars we see in the halo did not in fact form in say the same “clump” as those in the cluster core.

Another possibility is triggered star formation.

⁴ See the footprint at <https://www.galah-survey.org/news/announcing-galah-dr3>

⁵ Via datacentral.org.au/services/download, using the `sobject_id` identifiers.

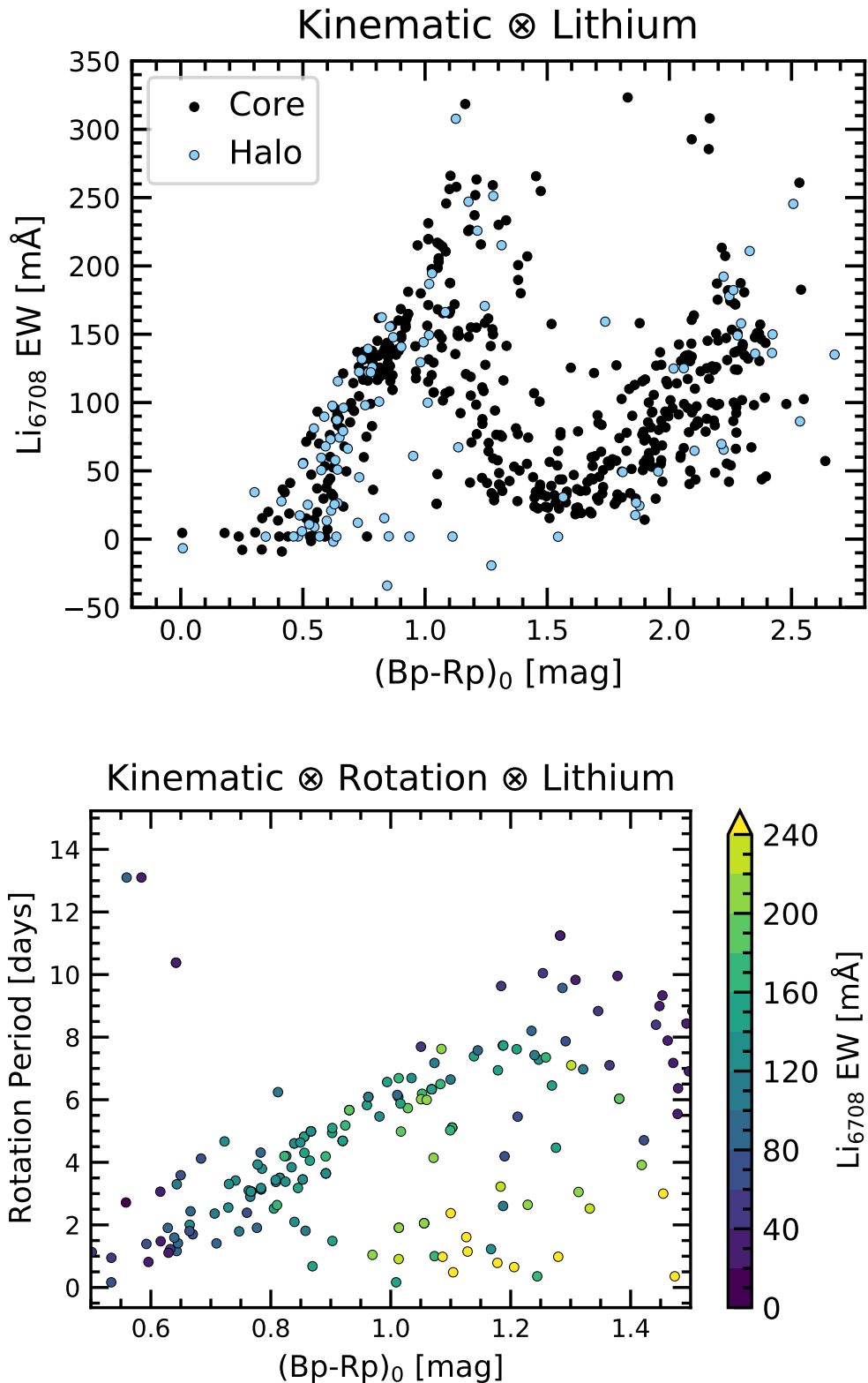


Figure 6. Lithium equivalent widths in NGC 2516, plotted against extinction-corrected color (*top*), and the combination of rotation period and extinction-corrected color (*bottom*). **TODO:** Do this against the autorot sample; Add the GALAH EWs

One relevant connection may be to the “Mamajek-2” stellar group (see Jilinski+2009).

4.2. Are the “very slow rotators” bona fide members?

Unsure. They are not isotropically distributed around the cluster... so either triggered star formation (CITE, CITE), or they’re actually field stars.

4.3. What is the contamination fraction in the halo? Does it change vs. location?

4.4. Mass differences between center and outer reaches?

4.5. Fast and blue rotators: are we going faster than other clusters?

4.6. Ways of doing this at different ages

Some final discussion is warranted on the applicability of our approach more generally. This work starts with a kinematically identified population, and then uses photometry (Gaia HR diagrams; TESS rotation) and spectroscopy (GALAH and Gaia-ESO lithium) to confirm youth in the stars. Other approaches are also possible.

One can start with photometric criteria (e.g., Gaia HR diagram of everything within some distance; Zari+18), or with spectroscopic criteria (CITE Berger+18), or with combinations thereof (e.g., CITE Zerjal 2019, 2020, Zhou’s work). It might even be possible to start using chemical abundance signatures (CITE, GALAHD3?).

These paths might in certain cases succeed in identifying more complete samples of dispersed members of young populations, since they do not require kinematic proximity.

5. CONCLUSION

We analyzed X, Y, Z. Our main results are as follows.

•

ACKNOWLEDGMENTS

The authors thank X and Y for fruitful discussions. L.G.B. and J.H. acknowledge support by the TESS GI Program, program NUMBER, through NASA grant NUMBER. L.G.B. was also supported by a XXXX Fellowship from Princeton University. This study was based in part on observations at Cerro Tololo Inter-American Observatory at NSF’s NOIRLab (NOIRLab Prop. ID 2020A-0146; 2020B-NUMBER PI: L. Bouma), which is managed by the Association of Universities for Research in Astronomy (AURA) under a cooperative agreement with the National Science Foundation. ACKNOWLEDGE PFS / CAMPANAS. This paper includes data collected by the TESS mission, which are publicly available from the Mikulski Archive for Space Telescopes (MAST). Funding for the TESS mission is provided by NASA’s Science Mission directorate. We thank the TESS Architects (George Ricker, Roland Vanderspek, Dave Latham,

Sara Seager, Josh Winn, Jon Jenkins) and the many TESS team members for their efforts to make the mission a continued success.

Software: astrobase (Bhatti et al. 2018), astropy (Astropy Collaboration et al. 2018), astroquery (Ginsburg et al. 2018), cdips-pipeline (Bhatti et al. 2019), corner (Foreman-Mackey 2016), IPython (Pérez & Granger 2007), matplotlib (Hunter 2007), numpy (Walt et al. 2011), pandas (McKinney 2010), scipy (Jones et al. 2001), wotan (Hippke et al. 2019).

Facilities: Astrometry: Gaia (Gaia Collaboration et al. 2016, 2018). Imaging: Second Generation Digitized Sky Survey, SOAR (HRCam; Tokovinin 2018). Spectroscopy: CTIO1.5m (CHIRON; Tokovinin et al. 2013), Photometry: TESS (Ricker et al. 2015).

REFERENCES

- Adams, F. C. 2010, *ARA&A*, **48**, 47, publisher: Annual Reviews
- Arancibia, J., Bouvier, J., Bayo, A., et al. 2020, Boletin de la Asociacion Argentina de Astronomia La Plata Argentina, 61C, 81
- Astropy Collaboration, Price-Whelan, A. M., Sipőcz, B. M., et al. 2018, *AJ*, **156**, 123
- Bailey, J. I., Mateo, M., White, R. J., Shectman, S. A., & Crane, J. D. 2018, *MNRAS*, **475**, 1609
- Baratella, M., D’Orazi, V., Carraro, G., et al. 2020, *A&A*, **634**, A34
- Bergond, G., Leon, S., & Guibert, J. 2001, *A&A*, **377**, 462
- Bhatti, W., Bouma, L., & Yee, S. 2019, cdips-pipeline v0.1.0, <https://doi.org/10.5281/zenodo.3370324>
- Bhatti, W., Bouma, L. G., & Wallace, J. 2018, astrobase, <https://doi.org/10.5281/zenodo.1469822>
- Bouma, L. G., Hartman, J. D., Bhatti, W., Winn, J. N., & Bakos, G. Á. 2019a, *ApJS*, **245**, 13
- Bouma, L. G., Winn, J. N., Baxter, C., et al. 2019b, *AJ*, **157**, 217
- Bouvier, J., Barrado, D., Moraux, E., et al. 2018, *A&A*, **613**, A63
- Bressan, A., Marigo, P., Girardi, L., et al. 2012, *MNRAS*, **427**, 127
- Buder, S., Sharma, S., Kos, J., et al. 2020, arXiv e-prints, 2011, arXiv:2011.02505
- Cantat-Gaudin, T., Jordi, C., Vallenari, A., et al. 2018, *A&A*, **618**, A93
- Cantat-Gaudin, T., Jordi, C., Wright, N. J., et al. 2019, *A&A*, **626**, A17
- Chen, Y., Bressan, A., Girardi, L., et al. 2015, *MNRAS*, **452**, 1068
- Chen, Y., Girardi, L., Bressan, A., et al. 2014, *MNRAS*, **444**, 2525
- Chen, Y., Girardi, L., Fu, X., et al. 2019, *A&A*, **632**, A105
- Choi, J., Dotter, A., Conroy, C., et al. 2016, *ApJ*, **823**, 102
- Cummings, J. 2011, PhD thesis, Indiana University
- Cummings, J. D., & Kalirai, J. S. 2018, *AJ*, **156**, 165
- Curtis, J. L., Agüeros, M. A., Mamajek, E. E., Wright, J. T., & Cummings, J. D. 2019, *AJ*, **158**, 77
- Davenport, J. R. A., & Sandquist, E. L. 2010, *ApJ*, **711**, 559
- Douglas, S. T., Agüeros, M. A., Covey, K. R., & Kraus, A. 2017, *ApJ*, **842**, 83
- Feiden, G. A., & Chaboyer, B. 2013, *ApJ*, **779**, 183
- Foreman-Mackey, D. 2016, *Journal of Open Source Software*, **1**, 24
- Freeman, K., & Bland-Hawthorn, J. 2002, *ARA&A*, **40**, 487
- Fukushige, T., & Heggie, D. C. 2000, *MNRAS*, **318**, 753
- Fürnkranz, V., Meingast, S., & Alves, J. 2019, *A&A*, **624**, L11
- Gagné, J., & Faherty, J. K. 2018, *ApJ*, **862**, 138
- Gagné, J., Faherty, J. K., & Popinchalk, M. 2020, *Res. Notes AAS*, **4**, 92
- Gagné, J., Roy-Loubier, O., Faherty, J. K., Doyon, R., & Malo, L. 2018, *ApJ*, **860**, 43
- Gagné, J., David, T. J., Mamajek, E. E., et al. 2020, *ApJ*, **903**, 96
- Gaia Collaboration, Prusti, T., de Bruijne, J. H. J., et al. 2016, *A&A*, **595**, A1
- Gaia Collaboration, Brown, A. G. A., Vallenari, A., et al. 2018, *A&A*, **616**, A1
- Ginsburg, A., Sipocz, B., Madhura Parikh, et al. 2018, Astropy/Astroquery: V0.3.7 Release
- Hippke, M., David, T. J., Mulders, G. D., & Heller, R. 2019, *AJ*, **158**, 143
- Hogg, D. W., Casey, A. R., Ness, M., et al. 2016, *The Astrophysical Journal*, **833**, 262
- Hunt, E. L., & Reffert, S. 2020, *A&A*, arXiv: 2012.04267
- Hunter, J. D. 2007, Computing in Science & Engineering, **9**, 90
- Jeffries, R. D., Jackson, R. J., Sun, Q., & Deliyannis, C. P. 2020, *MNRAS*, **500**, 1158, arXiv: 2010.04217
- Jones, E., Oliphant, T., Peterson, P., et al. 2001, Open source scientific tools for Python
- Kharchenko, N. V., Piskunov, A. E., Schilbach, E., Röser, S., & Scholz, R.-D. 2013, *A&A*, **558**, A53
- Kounkel, M., & Covey, K. 2019, *AJ*, **158**, 122
- Kounkel, M., Covey, K., & Stassun, K. G. 2020, *AJ*, **160**, 279
- Kounkel, M., Covey, K., Suárez, G., et al. 2018, *AJ*, **156**, 84
- Krumholz, M. R., McKee, C. F., & Bland-Hawthorn, J. 2019, *ARA&A*, **57**, 227
- Lada, C. J., & Lada, E. A. 2003, *ARA&A*, **41**, 57
- Lamers, H. J. G. L. M., Baumgardt, H., & Gieles, M. 2010, *MNRAS*, **409**, 305
- Mann, A. W., Gaidos, E., & Ansdell, M. 2013, *ApJ*, **779**, 188
- Marigo, P., Girardi, L., Bressan, A., et al. 2017, *ApJ*, **835**, 77
- McKinney, W. 2010, in Proceedings of the 9th Python in Science Conference, ed. S. van der Walt & J. Millman, 51
- Meingast, S., & Alves, J. 2019, *A&A*, **621**, L3
- Meingast, S., Alves, J., & Fürnkranz, V. 2019, *A&A*, **622**, L13
- Meingast, S., Alves, J., & Rottensteiner, A. 2021, *A&A*, **645**, A84
- Ness, M., Rix, H.-W., Hogg, D. W., et al. 2018, *The Astrophysical Journal*, **853**, 198
- O’Donnell, J. E. 1994, *ApJ*, **422**, 158
- Oh, S., Price-Whelan, A. M., Hogg, D. W., Morton, T. D., & Spergel, D. N. 2017, *AJ*, **153**, 257
- Pecaut, M. J., & Mamajek, E. E. 2016, *MNRAS*, **461**, 794
- Pérez, F., & Granger, B. E. 2007, Computing in Science and Engineering, **9**, 21
- Piskunov, A. E., Just, A., Kharchenko, N. V., et al. 2018, *Astronomy and Astrophysics*, **614**, A22
- Rajpurohit, A. S., Reylié, C., Allard, F., et al. 2013, *A&A*, **556**, A15
- Randich, S., Tognelli, E., Jackson, R., et al. 2018, *A&A*, **612**, A99
- Rebull, L. M., Stauffer, J. R., Bouvier, J., et al. 2016, *AJ*, **152**, 113
- Ricker, G. R., Winn, J. N., Vanderspek, R., et al. 2015, *Journal of Astronomical Telescopes, Instruments, and Systems*, **1**, 014003
- Röser, S., Schilbach, E., & Goldman, B. 2019, *A&A*, **621**, L2
- Shu, F. H., Adams, F. C., & Lizano, S. 1987, *ARA&A*, **25**, 23

- Soderblom, D. R., Jones, B. F., Balachandran, S., et al. 1993, *AJ*, **106**, 1059
- Spitzer, Jr., L. 1958, *ApJ*, **127**, 17
- Stauffer, J. R., Jones, B. F., Backman, D., et al. 2003, *AJ*, **126**, 833
- Tang, S.-Y., Pang, X., Yuan, Z., et al. 2019, *ApJ*, **877**, 12
- Tian, H.-J. 2020, *ApJ*, **904**, 196, publisher: American Astronomical Society
- Tokovinin, A. 2018, *PASP*, **130**, 035002
- Tokovinin, A., Fischer, D. A., Bonati, M., et al. 2013, *PASP*, **125**, 1336
- Wallace, J. J. 2018, *Res. Notes AAS*, **2**, 213
- Walt, S. v. d., Colbert, S. C., & Varoquaux, G. 2011, Computing in Science & Engineering, **13**, 22
- Wright, N. J., & Mamajek, E. E. 2018, *MNRAS*, **476**, 381
- Zari, E., Hashemi, H., Brown, A. G. A., Jardine, K., & de Zeeuw, P. T. 2018, *Astronomy and Astrophysics*, **620**, A172
- Zuckerman, B., & Song, I. 2004, *ARA&A*, **42**, 685

APPENDIX

A. CLUSTERING METHOD DETAILS

[CG18](#) applied a procedure that yielded what we call “the core”. Their procedure was to first query a Gaia DR2 cone around the previously reported RA and dec of the cluster, and within ± 0.5 mas of its previously reported distance. The outer radius of their cone was either r_2 from MWSC (CITE Kharchenko 2013), or twice the “cluster radius” listed by DAML/Dias (CITE). No proper motion cut was applied. They then applied an unsupervised classification scheme called UPMASK to $G < 18$ mag stars within this cone (CITE). The steps of UPMASK are first to perform a k-means clustering in the “astrometric space” $(\mu_{\alpha'}, \mu_{\delta}, \pi)$. Then, a “veto” step is applied to assess whether the groups of stars output from the k-means clustering are or are not more concentrated than a random distribution. This is implemented by “comparing the total branch length of the minimum spanning tree connecting the stars with the expected branch length for a random uniform distribution covering the investigated field of view”. “To turn this yes/no flag to a membership probability, [Cantat-Gaudin et al. \(2018\)](#) then redraw new values of $(\mu_{\alpha'}, \mu_{\delta}, \pi)$ for each source based on the listed value, uncertainty, and covariance. After a certain number of redrawings, the final probability is the frequency with which a given star passes the veto”. In the case of NGC 2516, this yielded a reported “ ± 50 ” within which half of the cluster members were found to be within 0.496° . When we selected candidate NGC 2516 members from the results of [CG18](#), we opted to include all candidate members with reported membership probability exceeding 10%. While this seems *a priori* low, our results (**SECTION XXX**) show that this “membership probabiltiy” severely underestimates the purity of the [CG18](#) sample for NGC 2516. Their false positive rate across the sample is more like 1-5%.

[KC19](#) applied a different unsupervised clustering method to the 5-dimensional Gaia DR2 data (omitting radial velocities, due to their sparsity). Their selection function (see their Section 2) yielded $\approx 2 \times 10^7$ stars, mostly within ≈ 1 kpc and typically with $G < 18$ mag. Their clustering algorithm, which was run on this entire stellar sample, was the “hierarchical density-based spatial clustering of applications with noise” (HDBSCAN, CITE McInnes17). The classical DBSCAN algorithm “identifies clusters as overdensities in a multi-dimensional space in which the number of sources exceeds the required minimum number of points within a neighborhood of a particular linking length ϵ . HDBSCAN does not depend on ϵ ; instead it condenses the minimum spanning tree by pruning off the nodes that do not meet the minimum number of sources in a cluster and reanalyzing the nodes that do. Depending on the chosen algorithm, it would then either find the most persistent structure (through the excess of mass method), or return clusters as the leaves of the tree (which results in somewhat more homogeneous clusters). In both cases it is more effective at finding structures of varying densities in a given data set than DBSCAN.” “The two main parameters that control HDBSCAN are the number of sources in a cluster and the number of samples. The former is the parameter that rejects groupings that are too small; the latter sets the threshold of how conservative the algorithm is in its considerations of the background noise (even if the resulting noisy groupings do meet the minimum cluster size). By default, the sample size is set to the same value as the cluster size, but it is possible to adjust them separately.” Regarding membership probabilities, [KC19](#) did not report continuous membership probabilities, instead opting for the binary “member” or “not”.

[M21](#) did the same as [KC19](#), but required A) the tangential velocity dispersions to be smaller, and B) deconvolved the distances.
FIXME **FIXME** **FIXME** **FIXME** **FIXME** **FIXME** **FIXME**

B. DETRENDING DETAILS

In “detrending” for our general variability search, our goal was to preserve astrophysical variability, while removing systematic variability. One particular concern for the TESS light curves is systematic variability at the timescale of the 14-day satellite orbit, mostly induced by scattered light from the Earth and Moon.

We therefore turned to the principal components (i.e., the eigenvectors) calculated following the procedure described by [Bouma et al. \(2019a\)](#). In brief, these vectors are computed using a set of “trend stars” selected from across each CCD according to ad-hoc heuristics that (hopefully) lead them to be dominated by *systematic* variability (Sec 3.7.2).

The principal component vectors, also referred to as the eigenvectors, are rank-ordered by the degree of variance that they predict in the training set (of “trend stars”).

We then posit that any given target star’s light curve is described as a linear combination of the eigenvectors. Optionally, we also considered the inclusion of additional systematic vectors that could affect the light curve, such as the CCD temperature, the flux level measured in the background annulus, and the centroid positions of the stars on the CCDs. These can be treated as additional “features” in the linear model.

To determine the coefficients of the linear model after the full set of eigenvectors (plus optionally “sytematic” vectors) had been assembled, we explored two possible methods: ordinary least squares, and ridge regression. Ridge regression is the same as ordinary least squares, except it includes an L2 norm with a regularization coefficient. The regularization coefficient that best applied for any given target light curve was solved for using a cross-validation grid search, using `sklearn.linear_modelRidgeCV` (CITE).

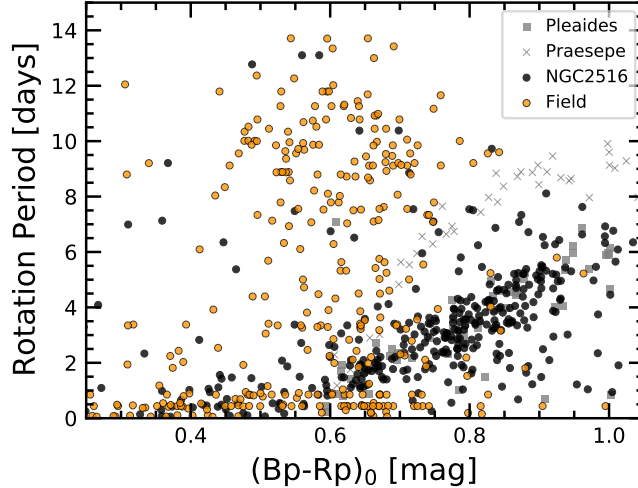


Figure 7. Rotation in NGC 2516 compared to the field. Stars with Gaia $Rp < 13$ mag in the cluster and field samples were considered. (Fainter stars in the field sample were not studied as part of the broader CDIPS project). The field stars show a different rotation period distribution than the kinematically selected NGC 2516 members.

Each target light curve was mean-subtracted and normalized by its standard deviation, as were the eigenvectors. The linear problem was then solved numerically, and the light curve was reconstructed by re-adding the original mean, and re-multiplying by the standard deviation to ensure that the variance of the light curve did not change.

We found that the choice of using ordinary least squares versus ridge regression did not seem to significantly affect the resulting light curves. In other words, the inclusion (or lack thereof) of a regularization term did not strongly alter the best-fitting coefficients. In the spirit of “KISS”, we opted to use ordinary least squares.

A few other choices seemed to be more important:

- *To smooth, or to not smooth the eigenvectors.* Ideally, the eigenvectors should be smooth in time. They should not contain residuals from *e.g.*, eclipsing binaries that snuck their way into the template set, and they should also not be intrinsically noisier than the target star. If either of these is the case (and we found that it sometimes was), it can induce extra variability into the PCA “detrended” light curves. To address this problem, we opted to smooth the eigenvectors using a time-windowed filter (with a “biweight” weight scheme, implemented in `wotan` by Hippke et al. (2019); window length 1 day, eval 6). One issue with this is that systematic sharp features (captured *e.g.*, in “spike vectors”) no longer are captured, so they end up in the “PCA detrended” light curves. They can then be filtered out (*e.g.*, using rolling outlier rejection), and we prefer this approach to having systematic features being *injected* by the PCA detrending.
- *How many eigenvectors to use.* A larger number always leads to greater whitening. In Bouma et al. (2019a), we performed a Factor Analysis cross-validation to determine the number of eigenvectors to use. The typical number adopted based on this analysis was 10–15. While this approach should in theory prevent over-fitting, in our experience, for stellar rotation it still often lead to distorts the signals, especially for rotation signals with small amplitudes and periodicities of $\gtrsim 3$ days. (Shorter signals typically are not distorted, since the eigenvectors do not contain the high-frequency content that leads to the distortions). For the present analysis, we therefore impose the maximum number of eigenvectors to be 5.
- *Which supplementary systematics vectors to use.* We considered using the BGV, CCDTEMP, XIC, YIC, and BGV vectors, packaged with the CDIPS light curves. We found that the background value measured in an annulus centered on the aperture, BGV, tended to produce the best independent information from the PCA eigenvectors, and so we adopted it as our only “supplementary” trend vector. We opted to not smooth it (in hopes that it would provide direct complement to the smoothed PCA vectors; 1 sharp vector containing literally the background information, plus 5 smooth vectors).

For every “target star”, we then decorrelated the raw (image-subtracted and background-subtracted) light curve using a linear model with ordinary least squares.

C. COMPARISON STAR ROTATION PERIODS

To provide a basis for comparison, we also opted to search the “calibration” light curves ($Rp < 13$) that were created as a part of the CDIPS project. Over the southern sky (Sectors 1–13 of TESS), this corresponded to a sample of 9,619,784 stars. Cross-matching these against the 13,843 randomly drawn stars in the neighborhood of NGC 2516 yielded 1,987 unique stars, with

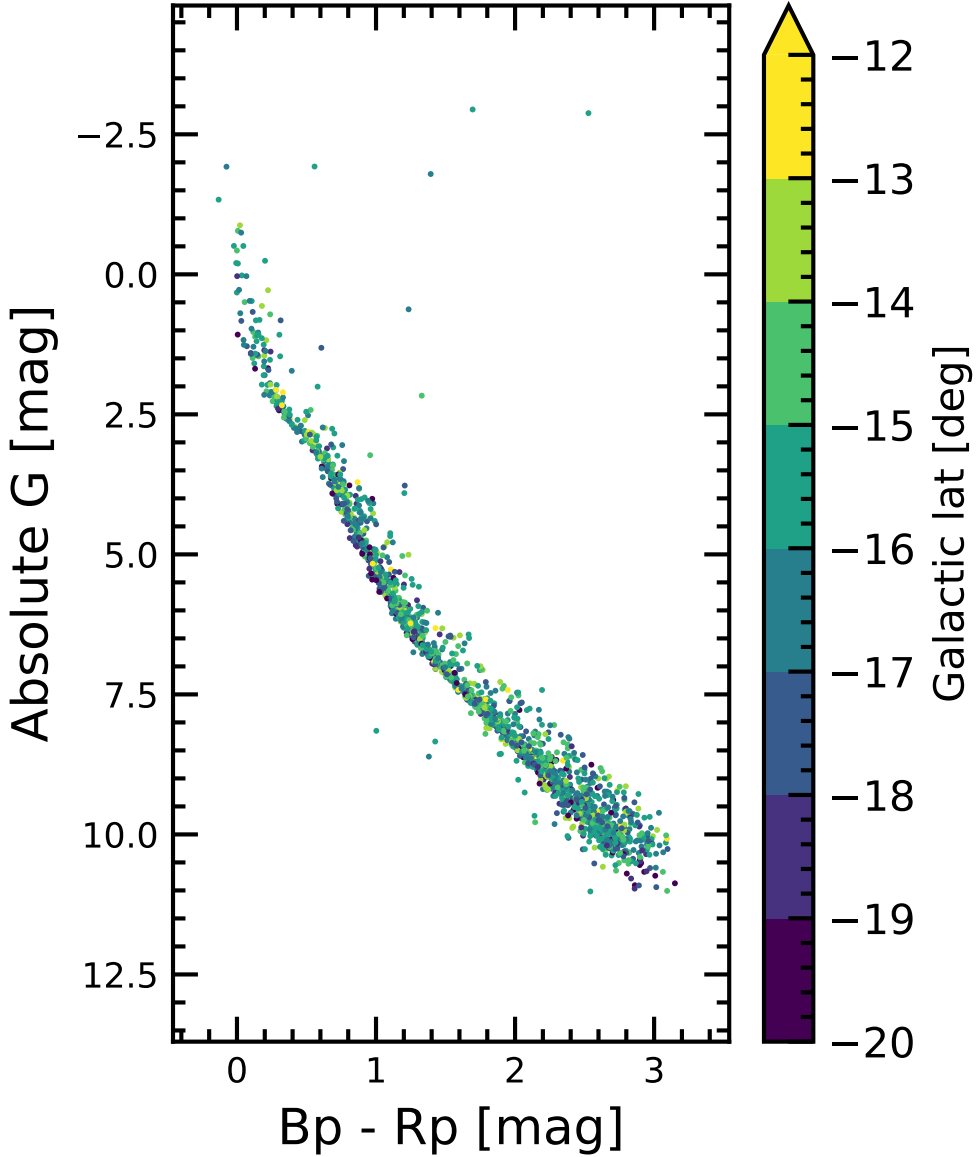


Figure 8. HR diagram of NGC 2516, using Gaia EDR3 photometry. Bottom: Reported members of the halo, as a function of galactic latitude. Can the additional scatter in the halo be understood through differential reddening? **Maybe.**

a cumulative total of 9,790 TESS sectors observed. The magnitude cut of $Rp < 13$ at the distances of the neighborhood sample corresponds to an extinction-corrected color cutoff of $(Bp - Rp)_0 \approx 0.80$, or spectral types of \approx G1V. This reaches sufficiently far down the main-sequence to enable a comparison to the cluster star sample.

We performed the same light curve stitching and period-search procedure on the field comparison stars. Imposing the same requirements for crowding resulted in 820 stars for which rotation periods could have been detected. Imposing the same Lomb Scargle power cutoff, and period upper limit, yielded 365 period detections (44.5%). Within the same brightness cutoff, 374 of 705 cluster stars yielded period detections (53.1%). Though the detection fractions are frankly not very different (likely because of the brightness cutoff), the period vs color distributions are quite different (Figure 7).

D. DIFFERENTIAL REDDENING

Figure 8.

E. ROTATION \otimes RUWE

Figure 9.

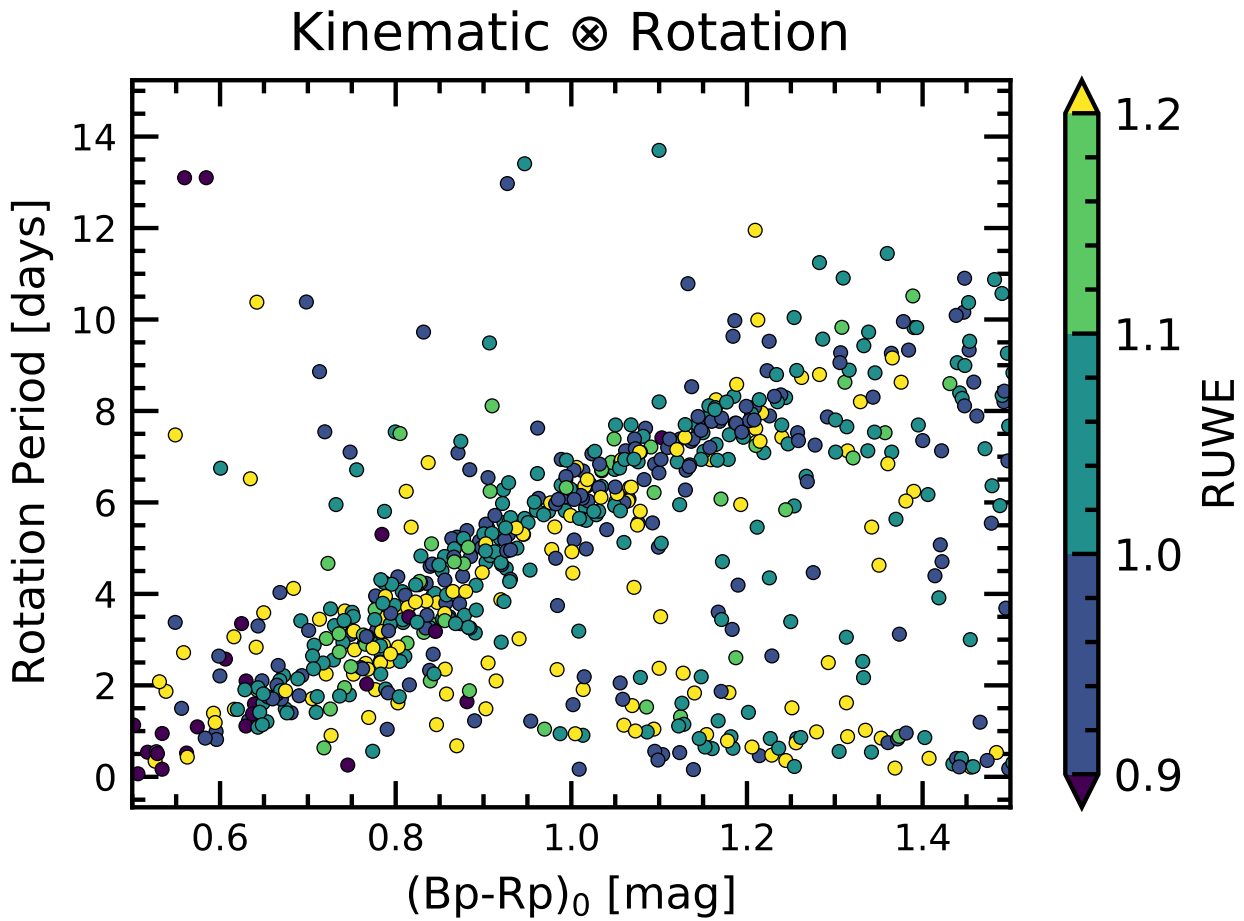


Figure 9. Rotation versus color, colored by RUWE. Looks like on the slow sequence, there's more yellow at the bottom?

F. KINEMATICS \otimes ROTATION IN EDR3

How did we do? Figure 10 lets us check with a more precise astrometric solution.

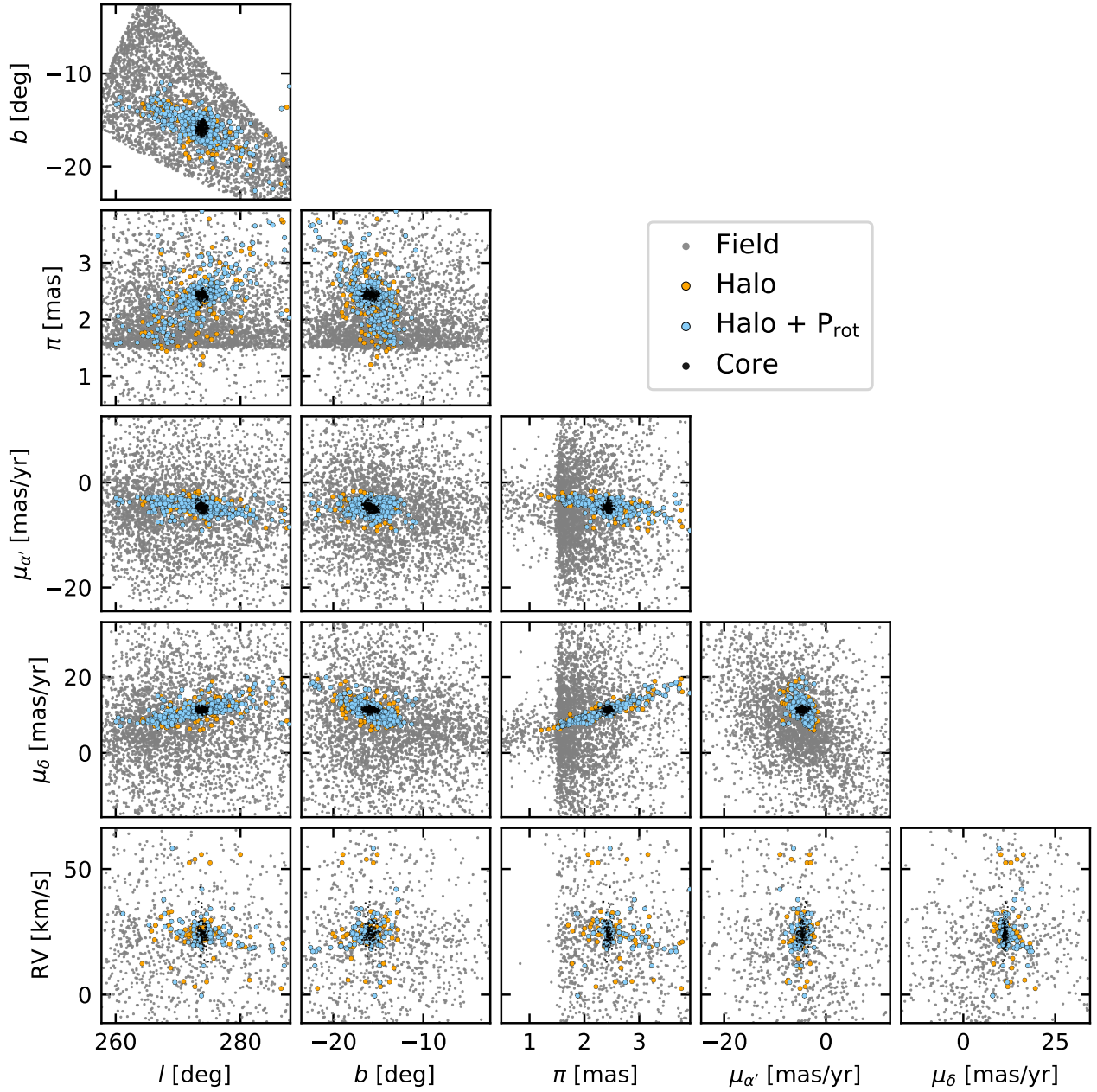


Figure 10. Gaia-based components of NGC 2516 in position and velocity space, cross-matched against the rotators. Analog of Figure 4, but showing EDR3 kinematics.